OPEN

Radiation Tolerance of Nanocrystalline Ceramics: Insights from Yttria Stabilized Zirconia

Sanchita Dey[1], John W. Drazin[1], Yongqiang Wang[2], James A. Valdez[2], Terry G. Holesinger[3], Blas P. Uberuaga[2] & Ricardo H. R. Castro[1]

[1]Department of Chemical Engineering and Materials Science & NEAT ORU, University of California, Davis, CA 95616, USA, [2]Materials Science and Technology Division, Los Alamos National Laboratory, Los Alamos, NM 87545, USA, [3]Materials Physics and Applications Division, Los Alamos National Laboratory, Los Alamos, NM 87545, USA.

Correspondence and
requests for materials
should be addressed to
R.H.R.C. (rhrcastro@
ucdavis.edu)

Materials for applications in hostile environments, such as nuclear reactors or radioactive waste immobilization, require extremely high resistance to radiation damage, such as resistance to amorphization or volume swelling. Nanocrystalline materials have been reported to present exceptionally high radiation-tolerance to amorphization. In principle, grain boundaries that are prevalent in nanomaterials could act as sinks for point-defects, enhancing defect recombination. In this paper we present evidence for this mechanism in nanograined Yttria Stabilized Zirconia (YSZ), associated with the observation that the concentration of defects after irradiation using heavy ions (Kr$^+$, 400 keV) is inversely proportional to the grain size. HAADF images suggest the short migration distances in nanograined YSZ allow radiation induced interstitials to reach the grain boundaries on the irradiation time scale, leaving behind only vacancy clusters distributed within the grain. Because of the relatively low temperature of the irradiations and the fact that interstitials diffuse thermally more slowly than vacancies, this result indicates that the interstitials must reach the boundaries directly in the collision cascade, consistent with previous simulation results. Concomitant radiation-induced grain growth was observed which, as a consequence of the non-uniform implantation, caused cracking of the nano-samples induced by local stresses at the irradiated/non-irradiated interfaces.

Nanocrystalline ceramics (below 100 nm) are expected to exhibit enhanced radiation resistance to amorphization[1–3] as compared to their bulk counterpart due to their increased interfacial areas in the form of grain boundaries. Interfaces are expected to act as effective sinks for radiation-induced defects, significantly hindering the accumulation of point defects[4,5]. The mechanisms behind this effect are still under debate, but it is proposed that interstitial defects created during damage events primarily move into the grain boundary and could return to the bulk material, annihilate vacancies (healing effect) and promote radiation tolerance[6]. Large interfacial areas found in nanocrystalline samples enable shorter diffusion distances for defect migration and an overall effective healing mechanism, explaining the enhanced radiation tolerance observed. For instance, nanocrystalline partially inverse spinel MgGa$_2$O$_4$ can tolerate doses up to 96 displacements per atom (dpa), while its bulk counterpart was amorphized by a dose of just 12 dpa[4].

On the other hand, from a thermodynamic point of view, the energy associated with the increased interfacial fraction in nanocrystals decreases the gap between the free energy of corresponding crystalline and amorphous phases[7]. That is, polymorphic stability diagrams for the nanoscale show that interfacial areas are critical in defining the relative stability of phases as a function of particle sizes[8–10]. For instance, the stability of amorphous ZrO$_2$ nanoparticles increases with decreasing particle size because of its relatively lower surface energy[9,11] as compared to the crystalline counter-parts (monoclinic, cubic and tetragonal). The same concept is applicable for bulk nanocrystalline compounds where the surface area is negligible but grain boundaries are predominant. In these cases, the total grain boundary energy increases as grains get smaller and the energy gap between these compounds decay with smaller grains where an analogy between bulk amorphous materials and nanocrystalline materials can be drawn in the limit of diminishing grain size[9,12]. Therefore, from a thermodynamic point of view, nanomaterials should be more prone to radiation induced phase transitions (to amorphize), but as demonstrated for MgGa$_2$O$_4$, the kinetics of self-healing can sometimes counter-balance this instability.

A model proposed by Shen[7] describes the simultaneous effects (kinetics and thermodynamics) governing defect generation and healing in nanomaterials during radiation damage. Because of the opposite dependences on the grain size, an optimal grain size range, in which the self-healing mechanism is occurring while the amount of grain boundary is not enough to significantly affect the system stability, has been proposed. However, the ideal grain size would be system-specific because it depends on the free energy of phase transition, the excess energy from grain boundaries, the free energy for defect formation, and kinetics of healing, a combination of data that is unfortunately rarely available in the literature, making it difficult to test this hypothesis.

Despite this predicted (and observed experimentally in some cases) advantage of nanocrystalline materials regarding radiation tolerance, even if within specific grain size ranges, such materials are strongly subject to radiation-induced grain growth. That is, radiation-induced defects can trigger grain boundary mobility with a resulting increase in the average grain size and a total decrease in the system's free energy. The exact mechanism by which this radiation-induced grain growth occurs is still unclear, but the impacts of radiation-induced grain growth suggest that any benefits of nanocrystals in terms of radiation tolerance will have a limited life-time in radioactive environments.

The goal of this work is to study the extent of ion radiation-induced damage in nanocrystalline dense 10 mol% yttria stabilized zirconia (10YSZ) ceramics to provide further understanding on the overall dependence of defect generation and self-healing on the grain size. To achieve this, systematic studies were conducted on bulk samples (in contrast to films) of 10YSZ with different grain sizes prepared by Spark Plasma Sintering (SPS) and exposed to high radiation doses. Yttrium content (10 mol%) was selected to be enough to provide a fully stabilized fluorite structure and to avoid parallel phase transitions that can also be induced by irradiation[13,14]. In the context of nuclear materials, the fluorite phase is of particular interest because important nuclear compounds, such as urania and plutonia, crystallize in this structure. Therefore, zirconia has been considered a candidate fuel matrix, which requires resistance to neutron exposure, gamma and beta radiation, fission damage, and other extreme conditions[15].

Several works have been reported on ion irradiation of fully stabilized zirconia[15–18] and an impressive radiation tolerance is consistently observed, making it clearly a candidate for applications in high radiation environments. For instance, no amorphization was observed in zirconia to levels of irradiation of at least 100 dpa[15,19] which is enough to cause amorphization of other ceramic materials already considered to show high radiation resistance, such as $MgAl_2O_4$, at similar irradiation spectrum[20,21]. Damage accumulation is however clearly observed for irradiation using Xe ions. As the fluence increases, three stages of damage accumulation could be identified in zirconia: the first involving the formation of isolated defect clusters; a second intermediate stage where damage increases rapidly; and a third stage where accumulation is retarded due to the overlapping of dislocations and lattice defects[15]. While the crystallinity was not compromised even at the highest doses, changes in mechanical properties are expected upon defect accumulation. For instance, softening of zirconia has been reported for YSZ irradiated with Xe[19,22] but only at high doses. At low doses, hardening was observed, consistent with other works using Al, Ar, Zr or As[15]. Further, nanocrystalline ZrO_2, irradiated with 4 MeV Kr at room temperature, showed less defect accumulation than single crystal ZrO_2[23]. However, no systematic study on the role of grain boundary density in stabilizing zirconia against radiation tolerance has been performed. In this paper we report unprecedented data on ion irradiation of nanocrystalline fully stabilized zirconia to understand the role of grain boundaries on defect concentrations under high radiation doses.

Methods

Experimental Procedures. Cubic 10 mol. % Y_2O_3 stabilized zirconia (10YSZ) nanoparticles were prepared by a modified co-precipitation technique[24]. In a typical procedure, an aqueous solution of $ZrO(NO_3)_2$ (Alfa Aesar, 99.9%) and $Y(NO_3)_3$ (Alfa Aesar, 99.9%) was added drop-wise into an excess solution of 1 M ammonia and the precipitates were washed with water. The precipitated hydroxides were then collected by centrifugation and dried at 120°C for 12 h. After calcination at 450°C for 2 h under air, nanocrystalline oxide was obtained. The as-synthesized nanopowder was characterized for phases and crystallite size using X-Ray diffraction on a Bruker AXS Instrument (Bruker AXS Inc., Madison, WI, model D8 Advance; CuK_α Radiation $\lambda = 1.5418$Å).

The nanopowder was consolidated to 5 mm diameter and roughly 1 mm thick pellets by using a SPS machine (SPS machine, model 825S, Syntex, Tokyo, Japan) at 950°C (measured by K-type thermocouple positioned inside the graphite die and close to sample) for 5 min under a uniaxial pressure of 600 MPa under vacuum). About 150 mg of the 10YSZ nanopowder were loaded in a 5 mm diameter graphite die. The powder-loaded die was inserted in to a 19 mm graphite die. Silicon Carbide (SiC) plungers and spacers were used to allow high pressures. Details about the procedure and parameters can be obtained elsewhere[25]. Because of the graphite die and vacuum in the SPS chamber, a graphite layer developed on the sintered pellet. The obtained pellets were polished to remove a carbon contamination layer from surface and further calcined at 700°C for 5 h under oxygen flow to allow oxidation of reduced areas induced by the atmosphere during sintering. Sintered pellets were characterized using Archimedes' method to measure the relative density and all of the pellets had relative densities above 95% of the theoretical density. Grain sizes were determined from XRD peak broadening using whole pattern profile fitting performed using the Jade 6.1 (MDI) software and further confirmed by transmission electron microscopy (TEM). Samples with different grain sizes were obtained by calcination of the as-sintered samples in a tube furnace to allow grain growth (25 nm, 38 nm, and 220 nm).

Surface polished pellets with three different grain sizes were irradiated with 400 KeV Kr^{++} ions to obtain a controlled irradiated layer. An ion fluence of 5.36 × 10^{16} ions/cm^2 was implanted, with a calculated peak damage rate of roughly 6 × 10^{-3} dpa per second. SRIM (Stopping and Range of Ions in Matter) full cascade simulations assuming 40 eV threshold displacement energies for all elements were used to estimate the peak damage for 10YSZ at 129 dpa[25]. Grazing-incidence x-ray diffraction (GIXRD) measurements were carried out using a Bruker AXS D8 Advanced diffractometer, CuK_α Radiation, θ-2θ geometry, and at an angle of incidence of 0.25° to allow characterization of the damaged area. Irradiated samples were prepared for TEM examination using Focused Ion Beam (FIB) method. The irradiated and non-irradiated microstructures were examined using JEOL JEM 2500SE and JEOL JEM 2100F/Cs operating at 200 KeV in Scanning (S)TEM modes.

Results

Figure 1 shows representative TEM images of the as-prepared (non-irradiated) YSZ pellets. The microstructures are consistent with the density measurements, suggesting high densities (>95%), and grain sizes of roughly 25, 38, and 220 nm. Interestingly, the large grained sample (220 nm) showed evident porosities located mostly at triple junctions (Figure 1c). These pores are attributed to the adopted manufacturing procedure. That is, because this sample was prepared by calcination of with an initial grain size of 25 nm, and given that grain boundaries are less dense as compared to bulk crystalline structures, once the grain boundary volume decreases as a result of grain growth; pores are naturally created. Figure 2 shows GIXRD patterns for the non-irradiated pellets. The patterns are consistent with cubic fluorite structure without any traces of monoclinic or tetragonal polymorphs. Broadening of the peaks are observed for the smaller grained samples and calculated crystallite sizes are 25, 38 nm, and >100 nm, consistent with the TEM image analysis.

GIXRD patterns for the 10YSZ samples after Kr^+ irradiation to 129 dpa are also shown in Figure 2. When compared to the pristine pattern (non-irradiated), the 25 nm pellets showed evident sharpening of the peaks, suggesting radiation-induced grain growth and a new, larger crystallite size of 35 nm. Moreover, no significant shifts of the cubic-fluorite peaks are observed and no obvious phase transitions are evident. Similarly, the 38 nm sample did not show significant changes in its pattern after irradiation except peak sharpening consistent with grain growth; the crystallite size after irradiation was 45 nm. On the other hand, the 220 nm pellet showed significant reduction in peak intensity after irradiation. Slight broadening at the base of the peaks could also be noticed. This is suggestive of the accumulation of defects affect-
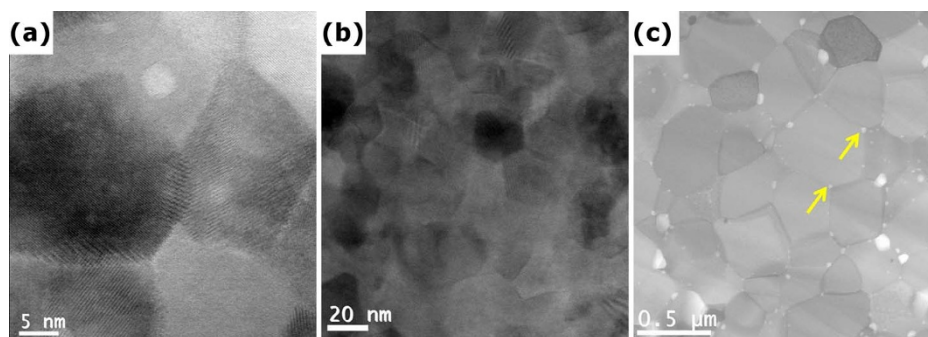
Figure 1 | STEM images of as-prepared pellets. STEM BF images as-prepared (non-irradiated) pellets: (a) 25 nm grained sample, (b) 38 nm grained sample and (c) 220 nm grained sample. The porosity of the largest grained sample in (c) is indicated by the arrows.

ing the x-ray scattering. However, no phase transition was observed and the fluorite structure remained intact, consistent with previous reports that show high radiation resistance of YSZ to amorphization.

Figure 3 shows a cross-sectional STEM Dark Field (DF) image of the irradiated 220 nm sample. The image is oriented such that the left side is the surface that was directly exposed to the beam. Two clear damage zones could be identified: an area showing small regions of brighter and darker contrast corresponding to irradiation damage, followed by an undamaged region at a depth of >230 nm. Figure 4 and 5 show cross-sectional STEM DF images for 25 nm and 38 nm grained 10YSZ samples, respectively. Beginning from the surface, the micrographs reveal an increase in grain size in the irradiated region, consistent with GIXRD data, followed by a severely-damaged region containing giant inter-granular cracks (that extended longitudinally throughout the sample), and an undamaged region at deeper regions. The grain size in the irradiated zone increased from 25 nm to 34.4 nm, and from 38 nm to 44.5 nm respectively, consistent with the measurements from GIXRD. Interestingly, the edge of the irradiated zone for both nanograined samples show much cleaner grains as compared to the large grained one, which is indicative of a smaller defect cluster concentration.

Figure 5a presents high magnification DF and BF images of the 220 nm sample. Two kinds of defect clusters are observed: bright zones in the STEM DF image suggest clusters comprised of higher thickness or accumulation of high Z elements (note that a high angle annular dark field (HAADF) detector was used for imaging and in a HAADF image, the intensity is proportional to square of Z, atomic number), while darker clusters suggest existence of vacancy rich zones. These clusters have reverse contrast in the BF images. Figure 5b and 5c shows higher magnification images supporting this same description and demonstrating that though the dark and bright areas have anisotropic shapes with sizes ranging from 5 to 10 nm, a closer look suggests that the clusters exist in small pockets of size 1–2 nm, and aggregate to form those large structures.

Figure 6a shows high magnification DF and BF images of the 25 nm grained sample – similar defect features have been seen in the high dpa zone of 38 nm grained sample. The defect clusters are all dark in the DF images for the nanograined samples (negligible bright clusters count), suggesting the defect clusters are comprised of the accumulation of vacancies in the small grained samples, as discussed further in the next session. Figure 6b and 6c shows the higher magnification BF and DF images of a representative damaged grain found in the nano sample. Consistently, dark spots of 1–2 nm are observed,
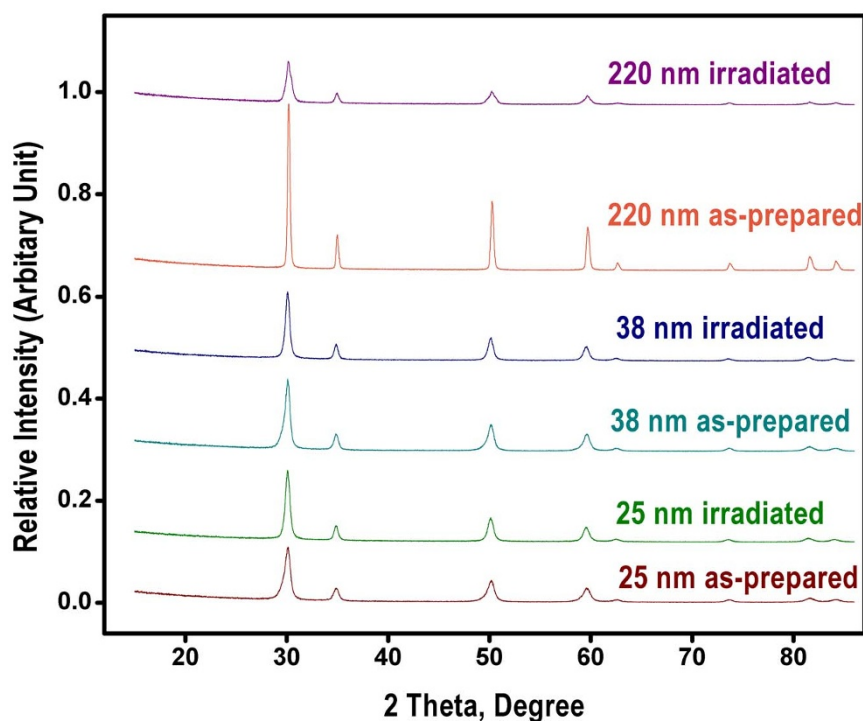
Figure 2 | GIXRD data. GIXRD patterns obtained from as-prepared and irradiated nano-crystalline 10YSZ samples.
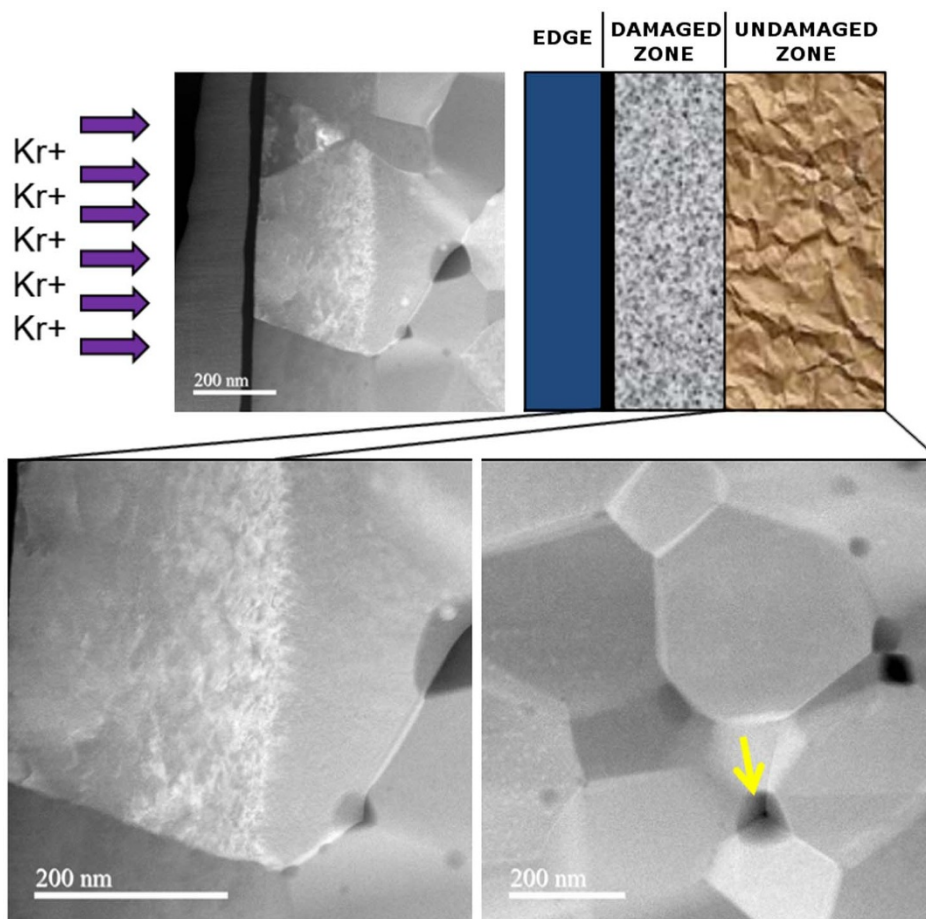
Figure 3 | STEM DF images for large grain sample. STEM DF images obtained from the irradiated 220 nm 10YSZ sample. The image on the top right is a schematic representation of the damaged and undamaged zones. Arrow in the STEM images indicate porosity not from irradiation but from sample preparation.

with absence of obvious bright spots. The clusters tend to aggregate much less as compared to the bulk sample though.

Quantification of damage was performed by calculating the concentration of defect clusters from high resolution STEM BF images using a standardized procedure as described elsewhere[23]. The number of both dark and bright 'spots' in the BF image (confirmed by DF image with reversed contrast) was counted. To facilitate counting, 1–2 nm diameter circles were used to delineate singular defect clusters (determined by observation) and the number of circles was counted encompassing areas of ~22500 nm^2 along the samples. Figure 7 shows the logarithm of the cluster concentration as a function of the logarithm of the initial grain size. The slope of the trend line is ~1.4, given the error bars, suggesting proportionality of defect concentration and grain size. However, the large error bars were a consequence of the small number of irradiated grains available in the TEM sample holder for analysis, compromising the quantitative reliability of this relationship.

Discussion

Due to the high energy of irradiation, the Kr^+ energy dissipates by exciting orbital electrons and by elastic collisions with the atomic nuclei in the YSZ structure. Elastic collisions may eject both cations and anions from their normal lattice position (primary knock-on) and a cascade of atomic displacements may occur before eventually coming to rest. Figure 8 schematically shows cationic and anionic vacancies and interstitials expected in YSZ. Since dealing with an ionic material, these defects may eventually cluster to reduce energy as a result of electrostatic interactions between defects, but a high concentration of defects can eventually lead to a loss of lattice periodicity, or amorphization.

The irradiation results for the nanocrystalline YSZ have a very distinct damage profile as compared to bulk YSZ. In neither case is amorphization observed despite the heavy ions used during irradiation and high levels of damage introduced (129 dpa), but the high magnification DF and BF images of the damage zones revealed distinct contrast patterns for the defect clusters. The presence of both bright and dark contrast in the DF image for the large grained sample indicates both an accumulation of high Z elements and an accumulation of vacancies. The bright areas suggest cation-rich defects (probably interstitials with high Z elements, Zr and Y) clusters, and indicate that diffusion to the grain boundaries is negligible; as a consequence of the smaller probability of a defect finding a grain boundary. Note these clusters can be stoichiometric or non-stoichiometric, but identifying the precise structure of these clusters is beyond the scope of this paper. The darker areas suggest the formation of vacancy clusters as well; indicating that vacancies do not migrate to boundaries during the time scale of the irradiation. These vacancies could be either cationic or anionic, but due to the high irradiation energy, it is likely that both kinds of defects co-exist and bind in low energy clusters due to electrostatic interactions.

In the nanograined samples, defects are more likely to find grain boundaries, which will then act as effective sinks, decreasing their net concentration, as shown in Figures 6 and 8. The absence of bright regions in the STEM DF images suggests cationic interstitials are not present but the darker regions suggest vacancy clusters do. A likely explanation for this damage profile is that cations excited during the
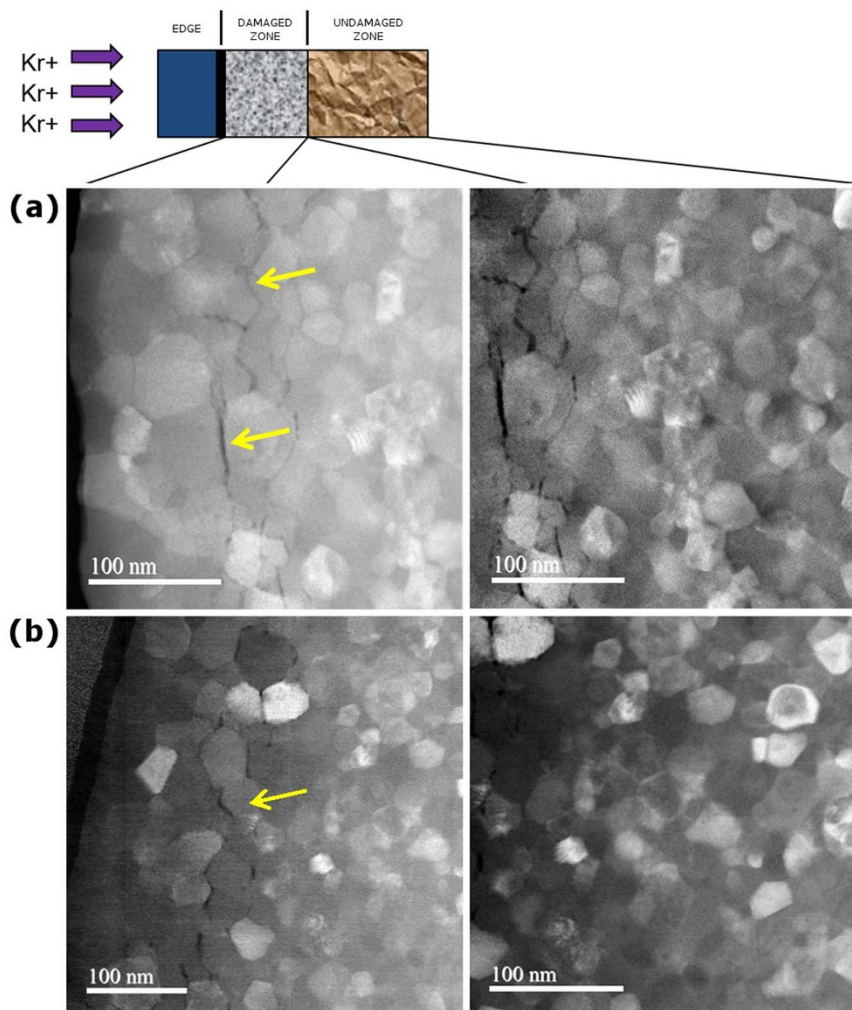
Figure 4 | STEM DF images for small grain samples. STEM DF images obtained from irradiated 38 nm (a) and 25 nm (b) 10YSZ sample. Arrows indicate intergranular cracks caused by grain coarsening in the irradiated zone.

cascade are immediately trapped by grain boundaries since grains are significantly small and mean distances are short[26]. The residual vacancies could then clusters as a consequence of their typically lower migration energy (in fluorite-structured materials, as opposed to many other oxides, vacancies tend to migrate faster than interstitials[27]) and highly exothermically clustering energy, that would result in lower energy as compared to isolated vacancies within the grain. The scenario is consistent with reduced interstitial-vacancy annihilation.

Another possible explanation for the different defect profiles is that not all defects have similar diffusivities, and therefore not all will be efficiently absorbed by the boundaries in equal fashion. In most ionic materials, vacancies are intrinsically less mobile than interstitials, especially at low temperatures such as that used in the present irradiation experiment (300 K)[4,7,28]. (note the temperature on the surface of the pellets during irradiation did not rise above 350 K). This would lead one to expect that in the nanograined samples the cationic interstitials would quickly migrate to the boundaries. Therefore, the defect clusters in the 25 nm and 38 nm grained samples should be mainly vacancy clusters (not interstitial clusters) which is consistent with the dark zones in the DF images for the nanocrystalline samples and the lack of the bright clusters observed for the large grained YSZ. However, for ZrO_2 and other fluorite structures, it has been reported that both cationic and anionic vacancies are faster than the corresponding interstitials[29]. Therefore, it is unlike this is the governing mechanism. This supports the hypothesis

above that interstitials are captured by grain boundaries directly in the collision cascades and not as a consequence of thermal migration.

On the other hand, the radiation induced grain growth observed in the nanograined YSZ can also lead to structural healing. Radiation-induced grain growth has been observed in other nanocrystalline samples, such as in CeO_2[30], metallic systems[31], and ZrO_2[32]. The driving force for grain growth is the elimination of the excess energy from the grain boundaries and reduction of local planar curvatures at the grain boundaries. The phenomenon is driven by defects, either temperature or radiation-induced[32], that allow increased migration kinetics of the boundaries towards concave curvatures. During irradiation, a high concentration of irradiation-induced point defects is expected through atomic collision cascades to accumulate in the sample and would then create mechanical instability in the crystal. In large grained samples, these defects are accommodated in the crystal, and the resulting strain cannot be relieved except with the formation of defect clusters. In nanocrystalline samples, the probability of a defect being "near" grain boundaries is much higher – "near" being defined as a shorter distance as compared to the mean diffusion path of a defect. Since the grain boundaries offer sinks for the oncoming defects, these radiation-generated defects tend to migrate to grain boundaries. The cooperative movement of defects will promote grain boundary migration; leading to grain growth.

The phenomenon of grain growth of the small grains is then somehow similar to a recrystallization process, where atoms from one grain (the smaller) move across a boundary and meet the other
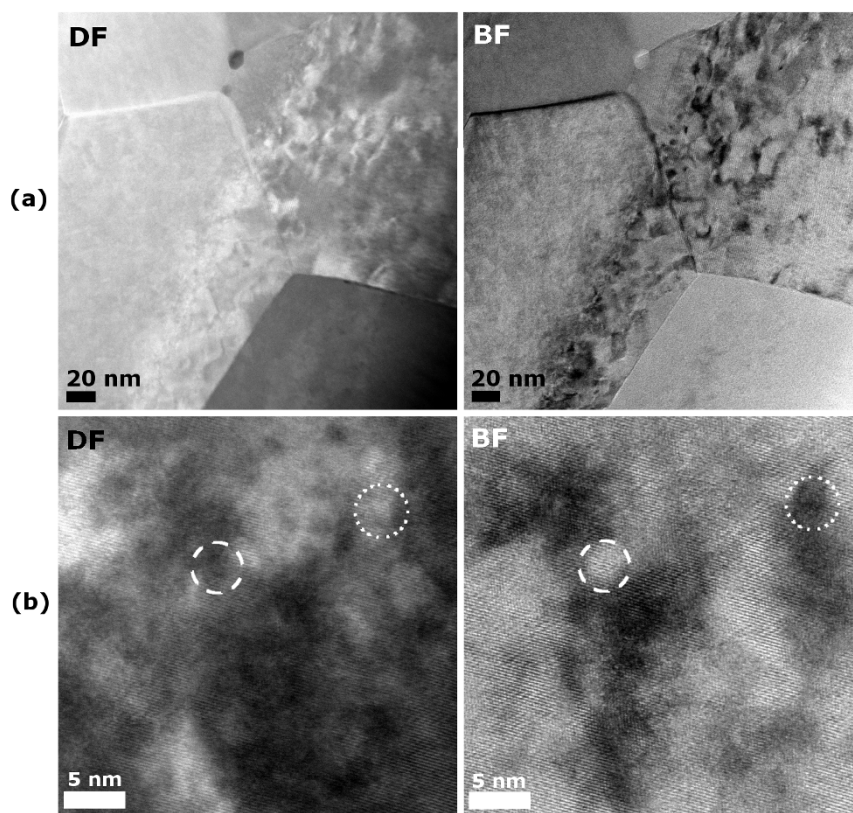
Figure 5 | STEM images for defect cluster large grain samples. STEM Dark Field (DF) and Bright Field (BF) images obtained from irradiated 220 nm sample. (a) Low magnification shows the division between damage and non-damage zones. Bright spots in DF indicate cationic clusters, which are dark in BF. Darker in DF are vacancy clusters, which are bright in BF. (b) Higher magnification indicating both kinds of defects clusters, as indicated by the circles.

grain (larger) and attach to its crystalline structure. This process ultimately leads to a decrease in the net defect concentration, since defects from one grain will not transfer to the other; hence, cleaner grains grow at the expense of smaller, defect concentrated grains[32]. However, the healing through this grain growth mechanism would leave no defects behind at all. The existence of vacancy clusters (dark zones in DF images) suggests this is not the dominate grain growth mechanism and supports the hypothesis that the grain boundaries are good sinks for interstitial defects.

Grain growth was however responsible for a catastrophic event that could ultimately limit application of nanomaterials under irradiation. For the two small grained samples, the edge of the irradiated zone is almost free from defects as they concentrate in the high dpa region, as shown in Figure 4. The accumulation of defects per se will also concentrate grain growth in that region, and as the grain size increases in the irradiated zone, residual stresses develop which may be the cause of the observed intergranular cracks at the interface between damaged and undamaged zones. No such cracks were observed at the interface of 200 nm sample because no significant grain growth occurs. The agreement of the cracking depth with the peak damage region predicted by SRIM suggests that cracking would be suppressed in irradiation environments where the dpa is more uniformly distributed, such as within a nuclear reactor. However, a parallel phenomenon seems inevitable when dealing with nanocrystalline samples, as radiation-induced grain growth proceeds the density of sinks diminishes invariably, limiting the utility of the material as radiation tolerant.

Model analysis

As previously discussed, a model has been proposed where a competition between the thermodynamics of nanocrystalline materials and kinetics of self-healing and defect generation play competitive roles in the overall radiation tolerance performance. It is of value to use the present data to quantitatively evaluate this concept. From a thermodynamic point of view, as the grain size decreases, there is a significant increase in the volume fraction of atoms associated within grain boundaries, which increases the free energy of the system. This increase may eventually allow the system to be dangerously close to the energy of the amorphous phase itself, facilitating amorphization upon irradiation. Quach and Castro have recently reported on the average grain boundary energy of 10YSZ[24], determining it to be 1.0 J.m^{-2}. The calculated Gibbs free energy for the total grain boundary volume in the 25 nm, 38 nm and 220 nm samples are therefore 2.48 kJ/mol (2482.78 m^2 of boundary per mol), 1.79 kJ/mol (1793.71 m^2 of boundary per mol) and 0.26 kJ/mol (263.81 m^2 of boundary per mol), respectively. As expected, the high values of grain boundary energy for smaller grained samples have a direct influence on grain growth. Aside from this, the excess energy brought to the system by the grain boundaries is fortunately still much below the energy difference between a cubic and an amorphous zirconia, which is roughly 20 kJ/mol, estimated using recent calorimetric data[9]. Figure 9 shows the increase in the free energy of the system referenced to the cubic fluorite polymorph as the grain size decreases. The energy of bulk transition to the amorphous phase is plotted for reference as a straight line at 20 kJ/mol. Note the energy for the nanograined samples will only cross the amorphous line near 3.3 nm, suggesting that crystalline samples with grain sizes below this value are unstable with relation to the amorphous phase even in non-irradiating environments. However, samples with grains larger than 3.3 nm should be thermodynamically stable.

Grain boundary thermodynamics is however only one aspect of the problem of irradiated nanocrystalline materials, and radiation-induced phase transition or radiation-induced amorphization in nano-grained materials is thermodynamically expected if[7],
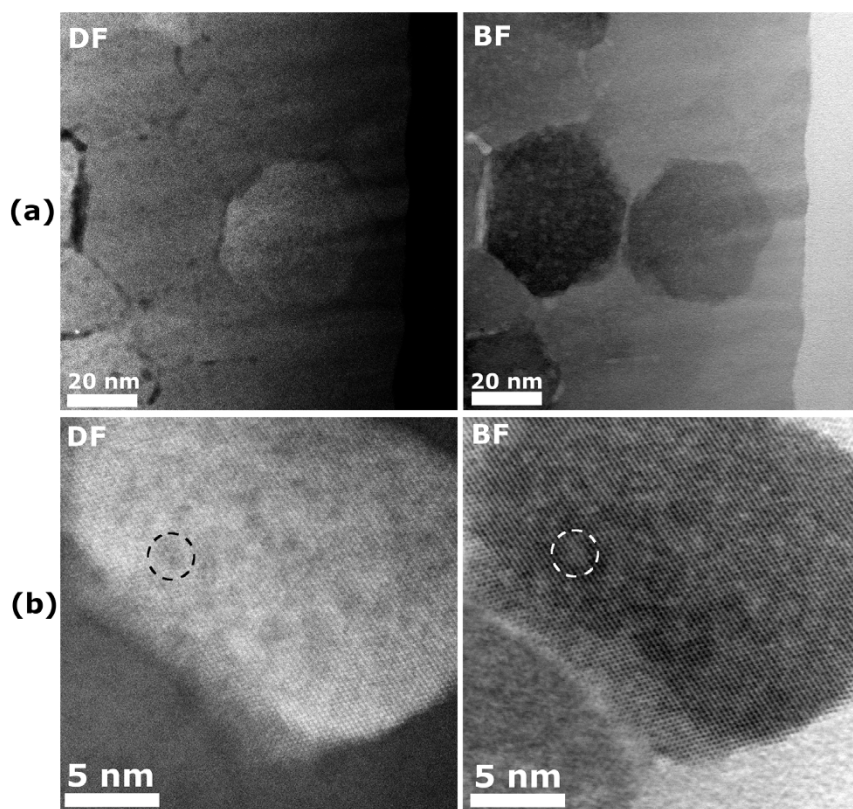
Figure 6 | STEM images for defect cluster small grain samples. STEM Dark Field (DF) and Bright Field (BF) images obtained from irradiated 25 nm sample. (a) Low magnification shows only dark spots in DF related to vacancy clusters, which are bright in BF. (b) Higher magnification indicates exclusively vacancy clusters, as indicated by the circles.

$$\Delta G_{gb} + \Delta G_{pd} > \Delta G_{pt} \qquad (1)$$

That is, if the excess energy from the grain boundaries (ΔG_{gb}) summed with the point defect energy (ΔG_{pd}) is larger than the energy of phase transition (ΔG_{pt}), then a phase transition would be thermodynamically favorable. The Gibbs free energy of point defects is however difficult to be predicted because it depends on the concentration of point defects, denoted by C. If vacancies are the main defects present in the system, then the variation of the free energy due to the presence of a vacancy concentration C_v can be described by[33]:

$$\Delta G_{pd} = C_v\left(\Delta H^f - T\Delta S^f\right) + k_B T[C_v ln C_v + (1 - C_v) ln(1 - C_v)] \qquad (2)$$

Where, ΔH^f is the formation enthalpy of a vacancy, T is temperature, k_B is the Boltzmann constant, ΔS^f ($\sim 2 k_B$)[34] is the entropy change for forming a vacancy and $k_B T[C_v ln C_v + (1-C_v) ln(1-C_v)]$ is the ideal entropy of mixing. Assuming defect annihilation is dominated by a grain boundary sink mechanism, it has been proposed that the concentration of vacancies and interstitials, for grain sizes below 100 nm, are given by[7]:
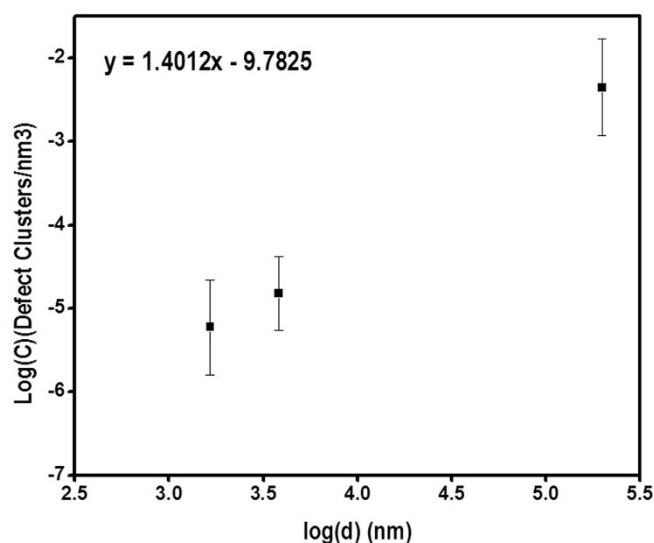
Figure 7 | Defect cluster concentration. Defect cluster concentration as a function of grain size for irradiated 10YSZ samples. The equation is for the regression fit of $C_{vd} = A \times d^n$ (where A and n are constants). Defect cluster concentration per area is calculated using a procedure used in the literature[23]. Relation $C_{vd} = C_{ad}^{3/27}$ is used to calculate the volume defect concentration.
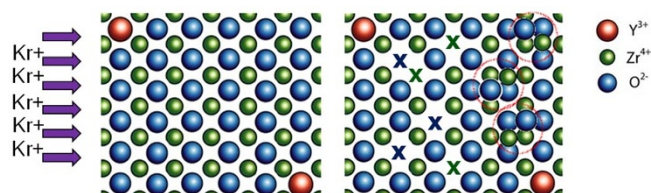
Figure 8 | Schematic of defect clusters formation mechanism in 10YSZ. Schematic of defect clusters formation mechanism in 10YSZ. "X" indicate vacancies with colors indicating their origin (cationic – green; anionic – blue). Red dotted circles point out interstitial defect clusters, with a higher local average Z.
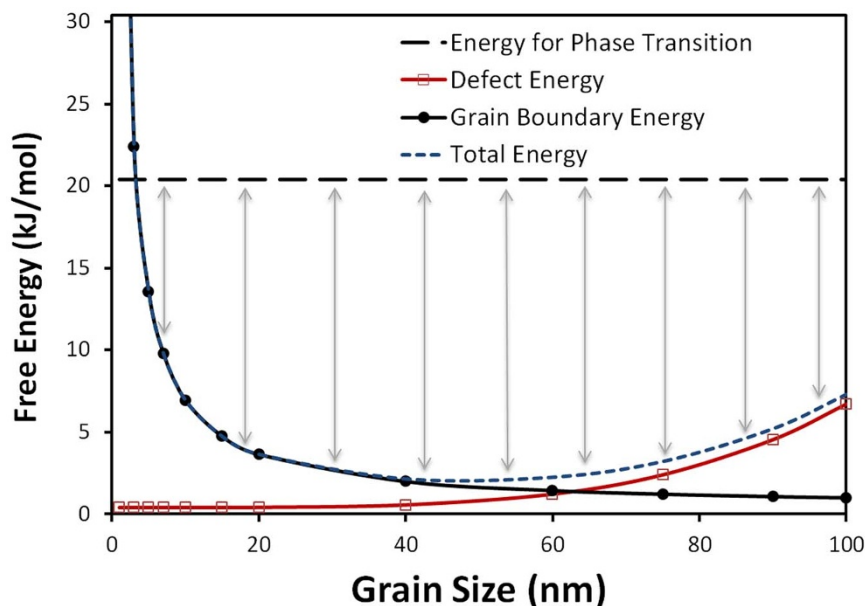
Figure 9 | Nanostablity diagram showing all energy associated with nano 10YSZ system. Energy of a nanocrystalline YSZ sample as a function of grain size with relation to the amorphous phase. Energy contribution from grain boundary increases as grain sizes decrease, and defect formation energy decreases with reducing grain size. Energy for amorphization (grey arrows) is affected by both, but for ultrafine grains is mostly affected by the boundary contribution.

$$C_V = \frac{K}{S_{gb}D_v} = \frac{Kd^2}{57.6D_v} \quad (3)$$

$$C_i = \frac{K}{S_{gb}D_i} = \frac{Kd^2}{57.6D_i} \quad (4)$$

where K is the atomic displacement rate, S_{gb} is the grain boundary sink strength, d is the average grain size, and D_i and D_v are diffusion coefficients for interstitials and vacancies, respectively. It has been reported in the literature that the prominent point defects in the grain interior of an irradiated nanostructure are basically vacancies because interstitials can easily migrate to the grain boundaries and recombine with vacancies located there[7,28,32]. In the case of YSZ reported here, given that irradiations were carried out at 300K, diffusivity in the system is practically null and the transport of interstitials to grain boundaries seems to occur directly in the collision cascades. In either case, the net result is an excess of vacancies in the grain interior.

This allows an analysis of post cascade defect recombination by using the above mentioned equations. Figure 7 shows a clear slope between defect concentration and grain size, but the not 2 as predicted by Shen's model[7], but 1.4. Unfortunately, the associated error bars do not allow further quantitative insights into this slope analysis, but assuming equation 3 holds true for YSZ with grain sizes below 100 nm, ΔG_{pt} was plotted in Figure 9 along with its sum and with ΔG_{gb}. ΔG_{pt} was calculated using D_v 1.2×10^{-16} cm^2.s^{-1}[35], a K value of 6×10^{-6} dpa.s^{-1} (according to simulations of our irradiation). The graph suggests the point defect energy does not significantly decrease the stability of nanocrystalline 10YSZ against irradiation, which is consistent with the lack of amorphous transition in our samples even after high radiation doses. The contribution of point defects slowly increases as the grain sizes increase, but cannot be responsible for amorphization even for samples with relatively large grain sizes (>100 nm).

Conclusion

High energy Kr$^+$ irradiation on nanocrystalline fully stabilized zirconia was performed to investigate the role of grain boundaries on damage evolution. No amorphization was observed, but large grained samples (220 nm) showed a higher concentration of defects as compared to nanograined ones (25 and 38 nm). Moreover, STEM images suggest that defects on large grained YSZ are composed of both vacancy and interstitial clusters, while for nanograined samples only vacancy clusters are observed. This indicates that interstitials can migrate to grain boundaries in the nanograined samples, and they work as effective defect sinks. Further, given the relative mobility of interstitials and vacancies in fluorite-structure crystals, this indicates that the transport of interstitials to the grain boundaries must occur directly in the collision cascades.

Grain growth was clearly observed in the nanograined samples, and was attributed to the coherent migration of radiation induced defects to the boundaries that caused grain boundary mobility to increase. Grain growth was not observed in large grained samples, indicating that the diffusion length of the defects is too small as compared to the grain size.

Finally, a thermodynamic analysis showed that the structural stability of the nanocrystalline YSZ under irradiation indicated strong resistance to amorphization. On the other hand, the observed grain growth lead to the formation of inter-granular crack between radiated and non-irradiated zones, which can be considered a major drawback for the radiation tolerance of nanomaterials at non-uniform irradiation conditions if not resolved.

1. Ackland, G. Controlling radiation damage. *Science* **327**, 1587–1588 (2010).
2. Misra, A., Demkowicz, M., Zhang, X. & Hoagland, R. The radiation damage tolerance of ultra-high strength nanolayered composites. *JOM* **59**, 62–65 (2007).
3. Samaras, M., Hoffelner, W. & Victoria, M. Irradiation of pre-existing voids in nanocrystalline iron. *J. Nucl. Mater.* **352**, 50–56 (2006).
4. Shen, T. D. *et al.* Enhanced radiation tolerance in nanocrystalline MgGa$_2$O$_4$. *Appl. Phys. Lett.* **90**, 263115 (2007).
5. Höchbauer, T., Misra, A., Hattar, K. & Hoagland, R. G. Influence of interfaces on the storage of ion-implanted He in multilayered metallic composites. *J. Appl. Phys.* **98**, 123516 (2005).
6. Bai, X. M., Voter, A. F., Hoagland, R. G., Nastasi, M. & Uberuaga, B. P. Efficient Annealing of Radiation Damage Near Grain Boundaries via Interstitial Emission. *Science* **327**, 1631–1634 (2010).
7. Shen, T. Radiation tolerance in a nanostructure: Is smaller better? *Nucl. Instr. Meth. Phys. Res. B* **266**, 921–925 (2008).

8. Castro, R. H. R. On the thermodynamic stability of nanocrystalline ceramics. *Mater. Lett.* **96**, 45–56 (2013).

9. Pitcher, M. W. *et al.* Energy crossovers in nanocrystalline zirconia. *J. Am. Ceram. Soc.* **88**, 160–167 (2005).

10. Costa, G. C. C., Ushakov, S. V., Castro, R. H. R., Navrotsky, A. & Muccillo, R. Calorimetric Measurement of Surface and Interface Enthalpies of Yttria-Stabilized Zirconia (YSZ). *Chem. Mater.* **22**, 2937–2945 (2010).

11. Ushakov, S. V. & Navrotsky, A. Direct measurements of water adsorption enthalpy on hafnia and zirconia surfaces using novel design for gas adsorption microcalorimetry. *Appl. Phys. Lett.* **87**, 164103 (2005).

12. Wu, N.-L., Wu, T. & Rusakova, I. A. Thermodynamic stability of tetragonal zirconia nanocrystallites. *J. Mater. Res.* **16**, 666–669 (2001).

13. Lu, F. *et al.* Phase Transformation of Nanosized ZrO_2 upon Thermal Annealing and Intense Radiation. *J. Phys. Chem. C* **115**, 7193–7201 (2011).

14. Balogh, A. G. Irradiation induced defect formation and phase transition in nanostructured ZrO_2. *Nucl. Instr. Meth. Phys. Res. B* **282**, 48–58 (2012).

15. Sickafus, K. E. *et al.* Radiation damage effects in zirconia. *J. Nucl. Mater.* **274**, 66–77 (1999).

16. Valdez, J. A., Chi, Z. H. & Sickafus, K. E. Light ion irradiation-induced phase transformation in the monoclinic polymorph of zirconia. *J. Nucl. Mater.* **381**, 259–266 (2008).

17. Sickafus, K. E. *et al.* Radiation damage effects in cubic-stabilized zirconia irradiated with 72 MeV I^+ ions. *Nucl. Instr. Meth. Phys. Res. B* **141**, 358–365 (1998).

18. Debelle, A. *et al.* Ability of cubic zirconia to accommodate radiation damage. *Scripta Mater.* **63**, 665–668 (2010).

19. Fleischer, E. L. *et al.* Microstructure of hardened and softened zirconia after xenon implantation. *J. Mater. Res.* **6**, 1905–1912 (1991).

20. Yu, N., Sickafus, K. E. & Nastasi, M. 1st observation of amorphization in single-crystal $MgAl_2O_4$ spinel. *Philos. Mag. Lett.* **70**, 235–240 (1994).

21. Sickafus, K. E., Yu, N. & Nastasi, M. Amorphization of $MgAl_2O_4$ spinel using 1.5 MeV Xe^+ ions under cryogenic irradiation conditions. *J. Nucl. Mater.* **304**, 237–241 (2002).

22. Fleischer, E. L., Hertl, W., Alford, T. L., Borgesen, P. & Mayer, J. W. The effect of ion induced damage on the hardness, wear and friction of zirconia. *J. Mater. Res.* **5**, 385–391 (1990).

23. Rose, M., Balogh, A. G. & Hahn, H. Instability of irradiation induced defects in nanostructured materials. *Nucl. Instr. Meth. Phys. Res. B* **127**, 119–122 (1997).

24. Quach, D. V. & Castro, R. H. Direct measurement of grain boundary enthalpy of cubic yttria-stabilized zirconia by differential scanning calorimetry. *J. Appl. Phys.* **112**, 083527 (2012).

25. Ziegler, J. F., Ziegler, M. D. & Biersack, J. P. SRIM - the stopping and range of ions in matter (2010). *Nucl. Instr. Meth. Phys. Res. B* **268**, 1818–1823 (2010).

26. Bai, X.-M. & Uberuaga, B. P. The Influence of Grain Boundaries on Radiation-Induced Point Defect Production in Materials: A Review of Atomistic Studies. *JOM* **65**, 360–373 (2013).

27. Malyi, O. I., Wu, P., Kulish, V. V., Bai, K. & Chen, Z. Formation and migration of oxygen and zirconium vacancies in cubic zirconia and zirconium oxysulfide. *Solid State Ionics* **212**, 117–122 (2012).

28. Uberuaga, B. P. *et al.* Dynamical simulations of radiation damage and defect mobility in MgO. *Phys. Rev. B* **71**, 104102 (2005).

29. Kilo, M. *et al.* Modeling of cation diffusion in oxygen ion conductors using molecular dynamics. *Solid State Ionics* **175**, 823–827 (2004).

30. Zhang, Y. *et al.* Structural modification of nanocrystalline ceria by ion beams. *Phys. Chem. Chem. Phys.* **13**, 11946–11950 (2011).

31. Kaoumi, D., Motta, A. T. & Birtcher, R. C. A thermal spike model of grain growth under irradiation. *J. Appl. Phys.* **104**, 073525 (2008).

32. Zhang, Y. *et al.* Grain growth and phase stability of nanocrystalline cubic zirconia under ion irradiation. *Phys. Rev. B* **82**, 184105 (2010).

33. Porter, D. A., Easterling, K. E. in *Phase Transformations in Metals and Alloys* Ch. 1, (Van Nostrand Reinhold (UK) Co., Ltd., 1981).

34. Wollenberger, H. J., Cahn, R. W., Haasen, P. *Physical Metallurgy.* Vol. 2 18 (Elsevier Science B.V, 1996).

35. Pornprasertsuk, R., Ramanarayanan, P., Musgrave, C. B. & Prinz, F. B. Predicting ionic conductivity of solid oxide fuel cell electrolyte from first principles. *J. Appl. Phys.* **98**, 103513 (2005).

Acknowledgments

Author contributions

S.D. performed sample preparations, microscopy and wrote the initial draft of the manuscript along with J.D. who provided further data analysis. Y.W. and J.V. performed irradiation experiments and GXRD analysis, respectively. T.H. and B.U. discussed scientific points of the paper and helped planning the experiments. R.C. wrote part of the manuscript and elaborated experiments. All authors reviewed the manuscript.

Additional information